Coherent Structure Eduction from PIV Data of an Electromagnetically Forced Separated Flow

T. Weier, C. Cierpka and G. Gerbeth

Forschungszentrum Dresden–Rossendorf, Magneto–Hydrodynamics Division
P.O. Box 510119, 01314 Dresden, Germany

Abstract. Periodic addition of momentum by wall–parallel electromagnetic forces has a strong influence on the separated region of a stalled airfoil. As in the case of periodic blowing and suction, actuation frequency and momentum input are the main factors of influence. However, the control authority depends as well on the actuation wave form. This latter aspect is investigated in the present paper by means of time resolved particle image velocimetry data from the suction side of an inclined flat plate. The control effect is rated by the size of the remaining recirculation region in the time averaged flow fields. The controlled flow possesses typically a small number of relatively large vortices, which are believed to be related to the control mechanism. Consequently, the time resolved flow fields have been analyzed by proper orthogonal decomposition and continuous wavelet transform to extract dominant features of the flow.

Key words: active flow control, proper orthogonal decomposition, continuous wavelet transform, waveform, coherent structures

1. Introduction

Flow separation control is a long standing topic in fluid mechanics research, since it has significant technological consequences. An overview of flow control including a comprehensive discussion of separation control can be found in [4]. Among the many methods available to control flow separation, the periodic addition of momentum to the separating flow is a relatively new one. Since it is often successful and requires for the same control goal, i.e. lift increase, typically much less momentum input than static actuation, periodic excitation has been intensively investigated during the last two decades. "Active flow control", a term now commonly used for periodic excitation, has been extensively reviewed by Greenblatt and Wygnanski [6], additional aspects can be found in the more recent overview by Seifert et al. [14]. Commonly, the excitation frequency and the time averaged momentum input are regarded as the key parameters for the control.
Seifert [13] characterizes actuation as the "primary enabling technology" for active flow control. Widely used actuation systems are, among others, loudspeakers, rotating valves connected to pressure sources and/or sinks, surface mounted Piezo benders, and Piezo fluidic actuators. In electrically conducting fluids, momentum input can be realized as well by electromagnetic, i.e. Lorentz forces. Lorentz force actuators do offer a number of attractive features: momentum is generated directly in the fluid without associated mass flux, the frequency response of the actuation is practically unlimited, no moving parts are involved. In the case of low conducting fluids and weak magnetic inductions, to which the present paper is limited, the force

is independent of the flow and can be easily computed from first principles. These advantages are, however, bought dearly by a low energetical efficiency, which is intrinsically coupled to the generation of Lorentz forces with strong electric and weak magnetic fields [15]. In spite of this, Lorentz force actuators are a valuable tool for basic research, and a considerable amount of experimental and numerical data on electromagnetic flow control in poorly conducting fluids has been collected. For a review, the interested reader may refer to [19].
The successful application of time periodic Lorentz forces to control separation at stalled airfoils has been shown experimentally in [18] and [1] and numerically in [10]. In the paper at hand, specifically the rôle of the actuation wave form for otherwise fixed parameters is discussed based on time resolved particle image velocimetry (TR–PIV) data. While actuation wave form effects have previously been observed in conventionally, see e.g. [9], as well as in electromagnetically excited [1, 18] separated flows, the underlying mechanism is not yet fully understood.

2. Experimental setup and parameters

Fig 1 shows the arrangement of flush mounted electrodes and permanent magnets which has been used to generate a wall parallel Lorentz force. This assembly was proposed by Gailitis and Lielausis [5]. The Lorentz force density

$$\mathbf{F} = \mathbf{j} \times \mathbf{B} \tag{1}$$

is the cross product of a current density $\mathbf{j}$ and a magnetic induction $\mathbf{B}$. As mentioned above and described in detail e.g. in [18], the current density distribution is independent of the flow in the case considered here. The electric as well as the magnetic fields have, apart from end effects, only components in wall normal and spanwise direction. Owing to Eq. (1) the Lorentz force distribution possesses a wall parallel component F_x only. The magnitude of the Lorentz force density is largest directly at the wall and decays exponentially with the wall distance. For further details and explanation, we refer to [18].
The forcing level is characterized by an effective momentum coefficient

$$c'_\mu = \frac{1}{2} \cdot \frac{aB_0}{\rho U_\infty^2} \cdot \frac{l}{c} \cdot \sqrt{\frac{1}{T} \int_0^T j(t)^2 \, \mathrm{d}t} \tag{2}$$

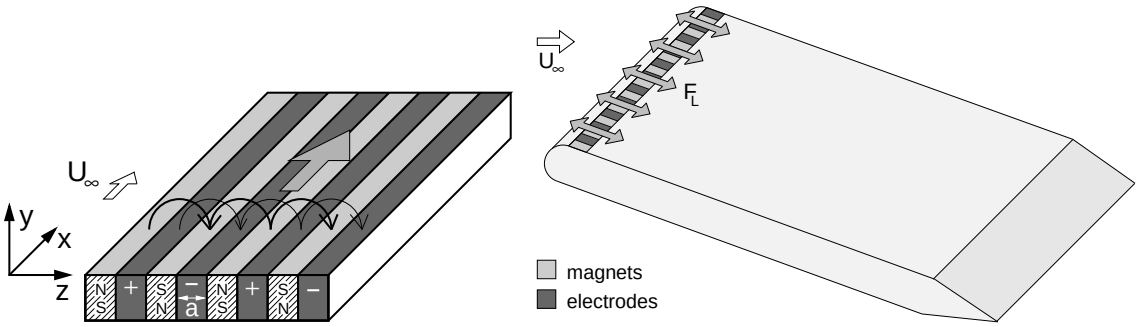

Figure 1. Electrode/magnet–array generating a wall–parallel Lorentz force in streamwise direction (left) and short electrode/magnet–array for time periodic forcing at the leading edge of the inclined plate.

relating the rms value of the total Lorentz force to a characteristic free stream momentum. In Eq. (2), a is the width of a single electrode or magnet and l its length. B_0 denotes the magnetic induction in wall normal direction measured at the magnets surface, $j(t)$ the current density depending on time t, and T the period of oscillation, respectively. As common practice (see, e.g. [6]), momentum coefficients are quoted in percentage terms for convenience.
The excitation frequency $f_e = 1/T$ is normalized using the chord length c and the free stream velocity U_∞:

$$F^+ = f_e c/U_\infty. \tag{3}$$

The plate was made of PVC and has a circular leading edge, a span width of 140 mm, a chord length of 130 mm, and a thickness of 10 mm. Electrodes and magnets have a width and length of $a = l = 5$ mm each. Plate shape and material were chosen as to allow for ease of manufacturing and durability in the electrolyte solution (0.25 M NaOH). The PIV measurements reported in the following were performed in a small electrolyte channel, driven by a centrifugal pump. A settling chamber with a free surface and equipped with a filter pad, two honeycombs and a set of four screens result nevertheless in a relatively small turbulence level in the test section. The latter, featuring a free surface as well, is 1 m long and has a 0.2×0.2 m cross section. To reduce end effects the plate has been mounted between rectangular plates with rounded edges made from PMMA extending from the bottom of the test section to the free surface in vertical and from 30 mm in front of the leading edge to 30 mm behind the trailing edge in horizontal direction. At the surface of the magnets, a mean magnetic induction of $B_0 = 0.35$ T was determined. A high power amplifier FM 1295 from FM Elektronik Berlin has been used to feed the electrodes. It was driven by a frequency generator Agilent 33220A.
The PIV setup consists of a Spectra Physics continuous wave Ar^+–Laser type 2020–5 as light source and a Photron Fastcam 1024PCI 100K to record the images. A thin ($\Delta z \approx 1$ mm) light sheet, formed by two cylindrical lenses, was placed at mid–span of the plate extending in the direction of the flow (x) and normal to the test section bottom (y). Since the laser was not shuttered, the camera was operated in shuttered mode at 60 Hz frame rate with a single image exposure time of 2 ms. For each parameter configuration a total of 6400 single images of 1024×512 pixel have been recorded synchronized to the excitation signal. For the seeding, polyamide particles (Vestosint) of 25 μm mean diameter were chosen. In the plane of the light sheet, x and y velocity components have been calculated from the images using PIVview–2C 2.3 from PivTec. Each image was correlated with its successor using multigrid interrogation with a final window size of 16×16 pixel^2 and 50% overlap, image deformation and sub pixel shifting was applied as well.

3. Data Postprocessing

Coherent structures have been educed from the time resolved velocity fields based on continuous wavelet transform (CWT) as well as on proper orthogonal decomposition (POD). It is neither intended nor possible to give a complete treatment of both approaches in the following. Instead, only the bare necessities to comprehend the results section are given.

3.1. Proper Orthogonal decomposition

POD is nowadays almost a standard technique to analyse flow fields. An overview can be found e.g. in [2].
Using velocity distributions as input, the resulting POD–modes $\Phi_k(x, y)$ are an optimal decomposition in terms of energy. The POD–modes used in the following are based on the vorticity ω (Eq. 4) and are therefore optimal in terms of enstrophy instead. The choice of vorticity distributions as input follows Kostas et al. [8] who have shown that the convergence of vorticity based POD–modes is prior to velocity based modes. Incidently the computational effort is reduced by a factor of two since only one variable per measurement point has to be analyzed. The snap shot method proposed by [17] has been applied to decompose the data sets using the eigenvalue routines provided by the GNU scientific library (GSL).
Since the separated flow over the inclined plate is relatively complex, the algorithm has been tested and verified to give reliable results for the well documented case of the flow around a circular cylinder.

3.2. Continuous Wavelet Transform

For the CWT, we followed the method proposed by [12]. A two dimensional Mexican hat wavelet has been used to transform time resolved vorticity fields calculated from the TR–PIV data. This approach allows the statistical evaluation of different vortex characteristics such as vortex size and circulation, trajectories and mean convection velocities. A comprehensive review of wavelet techniques for fluid mechanics is provided in [3].
In the following, some practical aspects of the implementation are given. The procedure follows closely that proposed by Schram [11], although the vortex detection here is based on the vorticity field

$$\omega = \frac{\partial v}{\partial x} - \frac{\partial u}{\partial y} \tag{4}$$

instead of the enstrophy field. u and v denote the velocity components in x- and y–direction, respectively. The vorticity field is in principle a well suited basis to detect vortices, since it is Galilean invariant. In order to discriminate between coherent structures and shear layers the λ_2–criterion as proposed by Jeong and Hussain [7] was used. Assuming two–dimensional, incompressible flow, the criterion reduces to

$$\lambda_2 = \left(\frac{\partial u}{\partial x}\right)^2 + \frac{\partial u}{\partial y}\frac{\partial v}{\partial x}. \tag{5}$$

Vortices are characterized by a negative λ_2. For regions of positive λ_2 the field has been set to zero. The wavelet analysis was later performed on this artificially generated vorticity field.
The two–dimensional Mexican hat wavelet is defined in polar coordinates as

$$\Psi\left(r, l\right) = \frac{1}{l}\left(2 - \frac{r^2}{l^2}\right)\ \exp\left(-\frac{r^2}{2l^2}\right) \tag{6}$$

with the wavelet scale l and the radius r. Again following Schram [11], the Lamb–Oseen vortex is assumed to be a representative model for the coherent structures.

The distribution of vorticity and tangential velocity u_ϕ

$$u_\phi(r) = \frac{\gamma}{2\pi r}\left[1 - \exp\left(\frac{r^2}{2\sigma^2}\right)\right] \tag{7}$$

$$\omega(r) = \frac{\gamma}{2\pi\sigma^2}\exp\left(\frac{r^2}{2\sigma^2}\right) \tag{8}$$

describing the Lamb–Oseen vortex is an exact solution of the Navier–Stokes equations. γ denotes the circulation, and σ the size of the vortex respectively.
The size of the vortex core D_K is usually defined by the maximum of the tangential velocity and hence is $D_\mathrm{K} = 3.17\sigma$ for the Lamb–Oseen vortex. Evaluating the wavelet coefficient for a Lamb–Oseen vortex, it is possible to relate the wavelet scale to the size of a corresponding Lamb–Oseen vortex as $l/\sigma = \sqrt{3}$
In order to determine the best possible choice for the wavelet scales the structure eduction algorithm computes the size of potential structures in advance and adjusts the range of scales which are used in the transformation. Applying this procedure allows for a more precise scale detection and saves computational time.

4. Results

4.1. POD modes

While the flow field has been measured at several angles of attack, momentum coefficients, and excitation frequencies, the following discussion will be limited to $c'_\mu = 2.6\ \%$, $F^+ = 1$ and an inclination angle of $\alpha = 13.5°$.
In the upper row of Fig. 2 the x–component of the velocity for the baseline flow as well as for the flow excited with two different wave forms are shown. One excitation has been generated by a time dependent current of a rectangular wave form with a duty cycle (DC) of one–third. The other excitation was produced by a triangular wave current. The DC=33% rectangular signal is referred to as "pulsed" in the following.
Regions of negative u, i.e. backflow, are drawn with dashed contour lines in Fig. 2 and indicate separation. It is clearly to be seen that separation is suppressed by excitation with both wave forms. However, some small differences in the flow near the surface of the plate are also visible. In the lower part of Fig. 2 the POD–modes 2–4 of ω are plotted, dashed contour lines identify negative values. The first mode of the POD belongs to the mean flow, since the total vorticity has been decomposed [16]. It is therefore not of interest for the eduction of the periodic characteristics of the flow. For the unforced case (left side) the vortex shedding modes 2 and 3 and the higher order vortex shedding modes are clearly visible. In the excited case the picture looks quite different. The mechanism for the reattachment of the mean flow is the momentum exchange between the outer flow and the separation region due to large scale vortex structures. Phase averaging shows a growth of such structures in the excitation region and a downstream movement as they separate from the evolving shear layer. These features can also be seen in the modes of the vorticity. The modes 2 and 3 are relatively similar for the different wave forms. However, modes 4 and 5 show smaller, but clearly distinguishable structures for the pulsed excitation. Due to the short duration of excitation, an additional natural shedding cycle occurs between

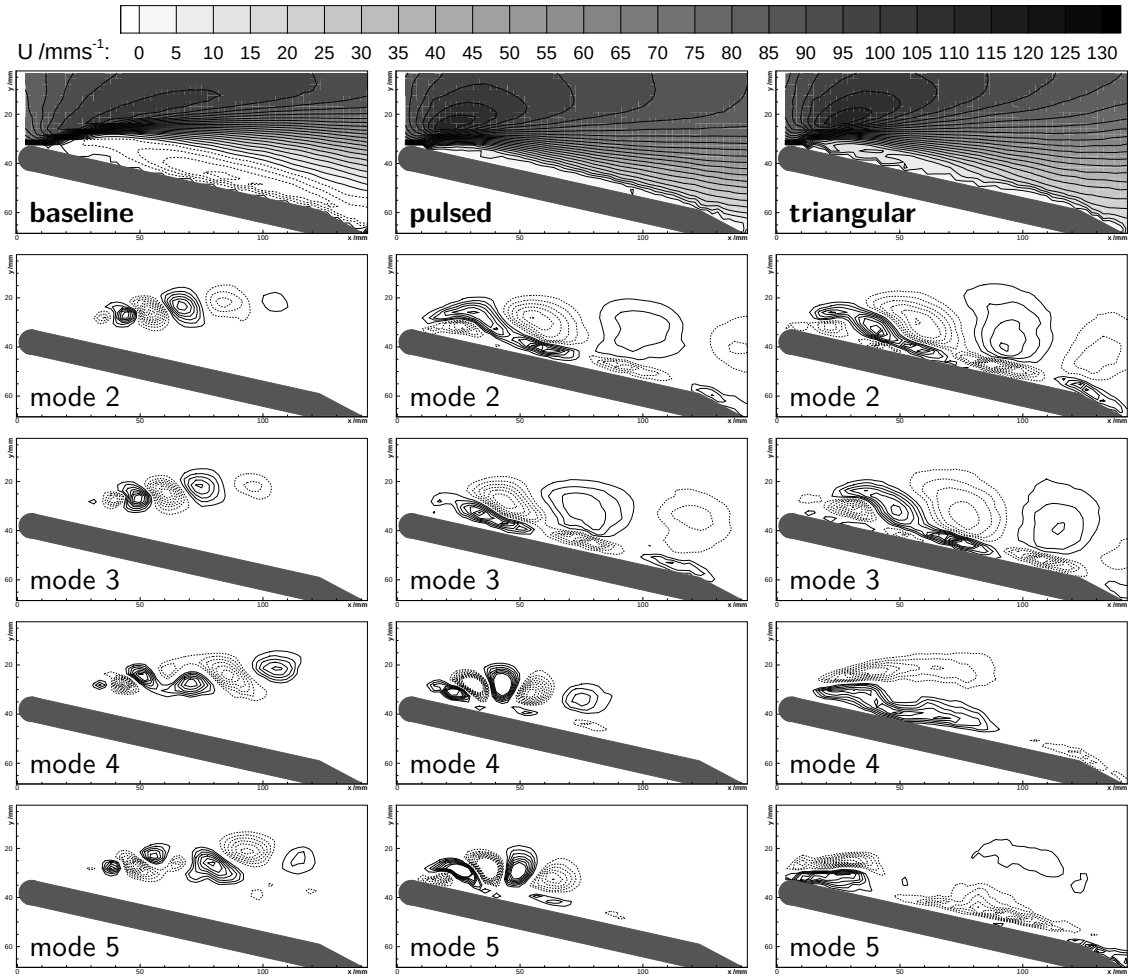

Figure 2. x–component of the velocity (top) and POD–modes 2 - 5 for the baseline (left), pulsed (middle) and triangular excitation (right).

the positive and negative part of the excitation signal. In the average, smaller structures are generated which disappear much faster than the vortex structures produced by the relatively gentle change of momentum input due to the triangular wave form. Note that the POD–modes do not indicate vortex structures, but are regions where significant features in terms of enstrophy content occur, meaning they correspond to regions of significant enstrophy and energy transfer.

Notable differences can also be seen in the energy fraction that each mode contributes to the overall dataset. For the flow around a circular cylinder with vortex shedding, the POD–modes occur, except of the mean mode, pairwise [2]. A similar behavior is clearly visible in Fig. 3 for the first modes of the baseline flow and the pulsed excitation. In the case of triangular excitation only mode 2 and 3 are paired. Since the Reynolds number is relatively high, $Re = 10^4$, giving rise to a broad bandwidth of flow scales, and probably caused as well by PIV resolution limits, the enstrophy content of the modes does not decrease as steep as for lower Reynold numbers and numerically determined data [8]. However, a shift of energy to higher modes which is originated by the excitation is clearly visible.

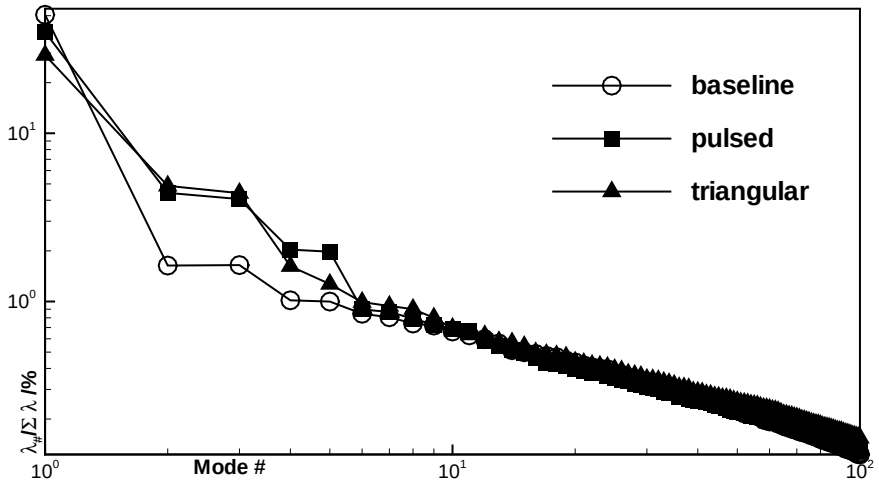

Figure 3. Energy fraction for the first 100 POD–modes for baseline (circles), pulsed (squares) and triangular excitation (deltas).

4.2. Vortex statistics using CWT

Using the CWT, vortices assumed to be similar to the Lamb–Oseen vortex are searched for in the PIV data of each time step. This approach leads to a large amount of data for each run containing position and characteristics of the detected vortices. In order to reduce the information content for the plots, the vortex parameters, including y–position, have been averaged for each streamwise location. The underlying discretization in streamwise direction is that of the PIV mesh.
In Fig. 4 the positions of the vortex centers are plotted versus the streamwise coordinate, yielding vortex trajectories in an averaged sense. For the baseline case, the vortices separate from the shear layer and move downstream where they get deformed and disappear slowly.

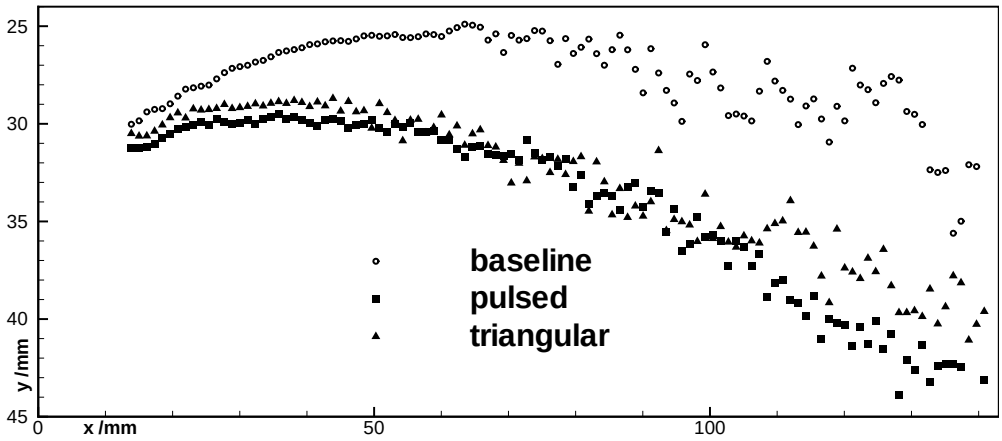

Figure 4. Vortex trajectories determined by the CWT analysis, y–direction stretched.

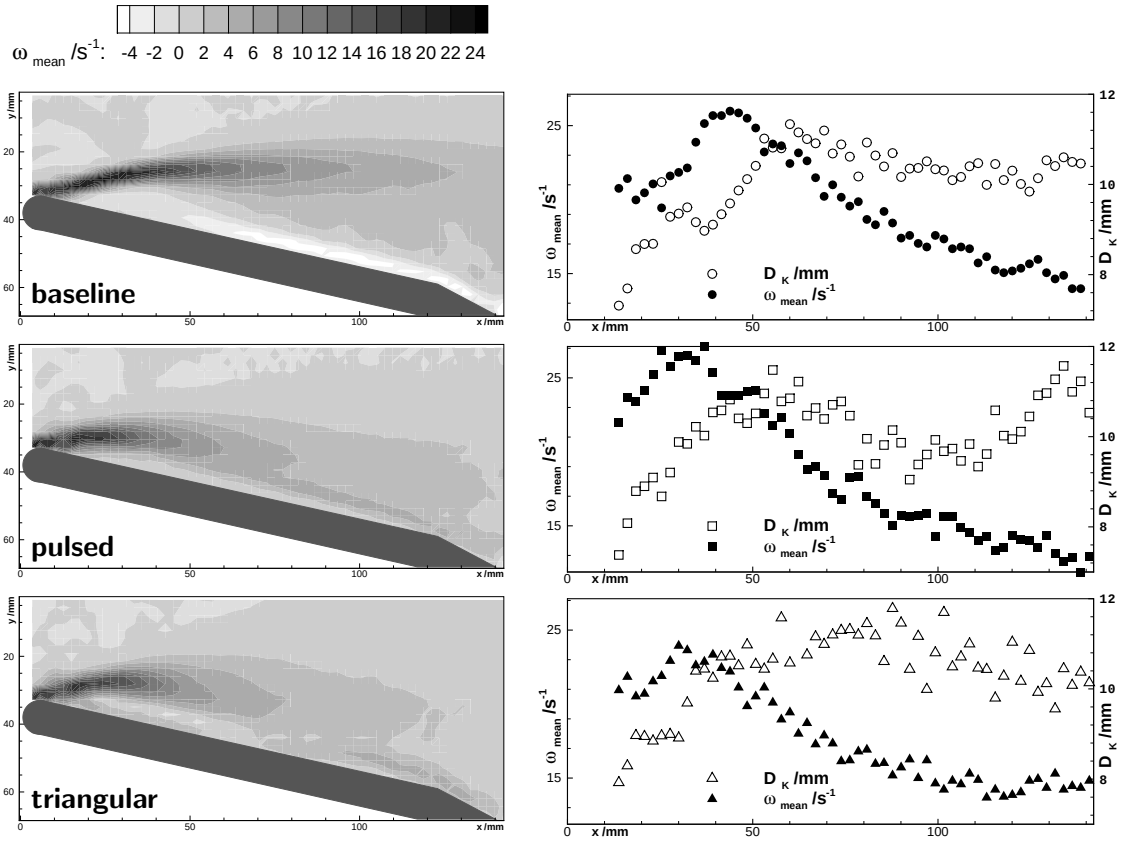

Figure 5. Time averaged vorticity (left), mean core diameter D_K and mean vorticity in the center of the detected vortices for the baseline (top), pulsed, and triangular excitation (bottom)

Under excitation with the pulsed wave form, small vortices are produced in the excitation region. In the off–phase of the signal, these vortices separate and are convected downstream near the surface of the plate. The trajectory owing to the triangle wave excitation is not as close to the plate as for the pulsed excitation. The likely cause for this observation is the comparatively slow change in momentum input. It allows for a shear layer to develop in the upstream forcing phase, but moves it away from the plate at the same time.

All trajectories show a considerable scattering of the points further downstream which is due to the fact that a smaller number of vortices is detected. Concurrently, the similarity of the deformed vortices to a Lamb–Oseen vortex wanes. More information about the effects of the excitation wave form can be extracted looking at, e.g., the size and core vorticity of the vortex structures. Fig. 5 shows the time averaged vorticity fields (left) and statistical averages of the vorticity in the center of a vortex (right, filled symbols) and of the vortex core size D_K (right, open symbols). The vorticity at the vortex center can be used as a measure for the energy content or intensity of a vortex structure. For the baseline flow, the vortices begin to grow in the shear layer. When they separate, the vorticity in the center diminishes while the size decreases slowly. The decay of the vorticity means that the energy of the structures dissipates and is transfered to the flow. The point for the maximum vorticity

of the vortices is shifted upstream due to the momentum input for the excited cases. Since the decay rate is of the same order as in the baseline flow, the momentum transfer takes place further upstream, suppressing the evolution of the separation bubble. For the pulsed wave form, smaller compact vortices are produced, visible in the higher vorticity as compared to the triangular excitation. As mentioned above in the off–phase of the actuator vortices are shed as well and are then convected downstream. In the phase with downstream directed Lorentz force, fast moving vortices are produced, while an upstream pointing force generates slower ones. This is a reason for the observed increase in vortex size, starting at $\approx 100\,\mathrm{mm}$ distance from the leading edge. The faster vortices catch the slower ones and they merge to a single large vortex. For the triangular excitation, large deformed structures are produced, reflected by the higher spread of the core diameter.

5. Conclusion

An apparent influence of the excitation wave form on coherent structures of the separated flow could be shown using POD as well as CWT of TR–PIV data. The tools used seem to be able to detect the flow characteristics and to highlight important features. Simultaneous TR–PIV and force balance measurements are scheduled for the near future in order to provide the necessary link of the educed flow structures to the resulting lift increase.

Acknowledgments

Fruitful discussion with Michael Hinze and financial support from Deutsche Forschungsgemeinschaft (DFG) in frame of the Collaborative Research Centre (SFB) 609 is gratefully acknowledged.

References

[1] C. Cierpka, T. Weier, and G. Gerbeth. Electromagnetic control of separated flows using periodic excitation with different wave forms. In *Active Flow Control*, volume 95 of *Notes on Numerical Fluid Mechanics and Multidisciplinary Design*. Springer, 2007. in press.

[2] L. Cordier and M. Bergmann. Proper orthogonal decomposition, an overview. In *VKI LS 2003-03, Post-Processing of Experimantal and Numerical Data*, Belgium, 2003. von Karman Institute for Fluid Dynamics.

[3] M. Farge. Wavelet transforms and their applications to turbulence. *Annual Review of Fluid Mechanics*, 24:395–457, 1992.

[4] Mohamed Gad-el Hak. *Flow control: passive, active, and reactive flow management*. Cambridge University Press, 2000.

[5] A. Gailitis and O. Lielausis. On a possibility to reduce the hydrodynamic resistance of a plate in an electrolyte. *Appl. Magnetohydrodynamics, Rep. Phys. Inst.*, 12:143–146, 1961. in Russian.

[6] D. Greenblatt and I.J. Wygnanski. The control of flow separation by periodic excitation. *Prog. Aero. Sci.*, 36:487–545, 2000.

[7] J. Jeong and F. Hussain. On the identification of a vortex. *Journal of Fluid Mechanics*, 285:69–94, 1995.

[8] J. Kostas, J. Soria, and M. S. Chong. A comparison between snapshot POD analysis of PIV velocity and vorticity data. *Experiments in Fluids*, 38:146–160, 2005.

[9] S. Margalit, D. Greenblatt, A. Seifert, and I. Wygnanski. Active flow control of a delta wing at high incidence using segmented piezoelectric actuators. In *1st Flow Control Conference*, St. Louis, MO, June 24–26 2002. AIAA–paper 2002–3270.

[10] G. Mutschke, G. Gerbeth, T. Albrecht, and R. Grundmann. Separation control at hydrofoils using Lorentz forces. *Eur. J. Mech. B Fluids*, 25(2):137–152, 2006.

[11] C. Schram. Application of wavelet transform in vortical flows. In *VKI LS 2002-04, Post-Processing of Experimental and Numerical Data*, Belgium, 2002. von Karman Institute for Fluid Dynamics.

[12] C. Schram, P. Rambaud, and M.L. Riethmuller. Wavelet based eddy structure eduction from a backward facing step flow investigated using particle image velocimetry. *Experiments in Fluids*, 36:233–245, 2004.

[13] A. Seifert. Closed–loop active flow control systems: Actuators. In *Active Flow Control*, volume 95 of *Notes on Numerical Fluid Mechanics and Multidisciplinary Design*. Springer, 2007. in press.

[14] A. Seifert, D. Greenblatt, and I.J. Wygnanski. Active separation control: an overview of Reynolds and Mach number effects. *Aerosp. Sci. Techn.*, 8:569–582, 2004.

[15] V. Shatrov and G. Gerbeth. Magnetohydrodynamic drag reduction and its efficiency. *Phys. Fluids*, 19(3):035109, 2007.

[16] S. Siegel, K. Cohen, J. Seidel, and T. McLaughlin. State estimation of transient flow fields using double proper orthogonal decomposition (DPOD). In *Active Flow Control*, volume 95 of *Notes on Numerical Fluid Mechanics and Multidisciplinary Design*. Springer, 2007. in press.

[17] L. Sirovich. Turbulence and the dynamics of coherent structures part I: Coherent structures. *Quarterly of applied mathematics*, 45:561–571, 1987.

[18] T. Weier and G. Gerbeth. Control of separated flows by time periodic Lorentz forces. *Eur. J. Mech. B/Fluids*, 23:835–849, 2004.

[19] T. Weier, V. Shatrov, and G. Gerbeth. Flow control and propulsion in weak conductors. In S. Molokov, R. Moreau, and H.K. Moffatt, editors, *Magnetohydrodynamics. Historical Evolution and Trends*. Springer, 2007. in press.